Impact of Cr Substitution on Structural, Magnetic, Electric and Impedance Study of Mn-Ni-Zn Ferrites

Shanzida Haque[1], Sajal Chandra Mazumdar[1*], Mohammed Nazrul Islam Khan[2], Mithun Kumar Das[1]

[1]Department of Physics, Comilla University, Cumilla, Bangladesh
[2]Material Science Division, Atomic Energy Centre, Dhaka, Bangladesh
Email: *sajalf@yahoo.com

Abstract

A series of Cr^{3+}-substituted Mn-Ni–Zn ferrites; $Mn_{0.5}Ni_{0.1}Zn_{0.4}Fe_{2-x}Cr_xO_4$ ($x = 0.0$ - 0.4 in a step of 0.1) were prepared by traditional solid-state reaction route. The structural, magnetic, dielectric properties and impedance spectroscopy of these compositions were studied. Phase identification and lattice constant (a_0) determination were carried out by X-ray diffraction (XRD). The XRD patterns established the fabrication of a single-phase spinel structure. The FESEM micrographs exposed that the average grain size ($\overline{D}$) increased slightly with chromium (Cr) substitution and then decreased for a higher concentration of chromium in the composition. The real part of initial permeability (μ_i') diminished owing to the enhanced porosity of the compositions with the increase of Cr^{3+} content in the composition. The highest relative quality factor (RQF) was attained for the samples with $x = 0.1$. The magnetic hysteresis was investigated to know the effect of Cr^{3+} substitution in the composition of the magnetic properties. The decrease of saturation magnetization (M_s) with an enhancement in Cr^{3+} might be triggered by switching of Fe^{3+} ions from octahedral to tetrahedral site. The samples with $x = 0.1$ exhibited the highest anisotropy constant (K). Curie temperatures of the investigated samples were significantly modified to lower temperatures with the Cr^{3+} content. The frequency characteristics of dielectric properties and impedance spectroscopy had been investigated. The highest dielectric constant (ε') and resistivity were observed for $x = 0.1$ and $x = 0.2$ samples. The complex impedance spectra analysis reveals in-depth information about the conduction mechanism, microstructure, and orientation of the grains in the samples.

Keywords

X-Ray Diffraction, Permeability, Dielectric Property, Curie Temperature,

Impedance Spectroscopy

1. Introduction

During the last few decades, ferrites are materials of great interest owing to their notable magnetoelectric properties. According to the structure, they have tetrahedral A-site and octahedral B-sites in the AB_2O_4 crystal lattice. These materials exhibit diverse magnetic and electrical properties subject to their cation distribution of the chemical compositions. Numerous cations could be located on the A-site and B-sites to modify their magnetic properties [1] [2] [3] [4]. Sivakumar *et al.* [1] studied the effect of milling, grain size, frequency, and temperature on the dielectric properties of nanocrystalline Ni-Zn ferrites. They found an unusual rise in dielectric loss with milling resulting from increased electrical conductivity due to oxygen vacancies introduced upon milling. On the other hand, the relaxation frequency was observed to decrease with milling due to increased interaction between charge carriers. Hossain *et al.* [2] observed that with the increase in Zn content in Ni-ferrite the Curie temperature (T_c), resistivity, and the activation energy dropped off whereas the magnetization, initial permeability, and the relative quality factor (Q) increased. A Hopkinson peak was obtained near T_c in the real part of the initial permeability vs. temperature curves. Chukalkin *et al.* [5] [6] and Mahmud *et al.* [6] observed the effect of Zn substitution on the magnetic properties Ni-Zn ferrites. Local angular structures of spin were evident for $x = 0.45$ with effective sizes of 1 - 10 nm [5] [6]. Rezlescu *et al.* studied the effect of divalent ions [7] and rare earth ions [8] on the structural, magnetic and electric properties of Ni-Zn ferrites.

From the functional viewpoint, Mn-Zn along with Ni-Zn ferrites epitomizes the most significant types. These are utilized in various ferrite devices for instance converters, inductor cores, electromagnetic wave absorbers, recording heads, etc. Mn-Zn ferrites own high μ_i' and magnetization but these are not appropriate for magnetic uses at higher frequencies owing to their high electrical conductivity and excessive power losses. In contrast, Ni-Zn ferrites have giant resistivity, small-dielectric loss ($\tan\delta_E$), and high Curie temperature (T_C), but they have somewhat minimal μ_i' at higher frequencies. Several authors considered the mixture of these two ferrites to obtain encouraging magnetic characteristics with moderate losses particularly in the excessive frequency range [9] [10] [11] [12]. In earlier studies, the magnetic and electrical effects of this sort of mixture were evaluated [12] [13]. The composition $Mn_{0.5}Ni_{0.1}Zn_{0.4}Fe_2O_4$ was found to possess the optimum magnetic characteristics for auspicious functions [12] [14] [15]. Preferential occupation of Cr^{3+} ions by octahedral sites in Ni-Zn ferrites replaces Fe^{3+} ions limiting Fe^{2+}-Fe^{3+} hoping conduction and increases resistivity. Accordingly, in the present work, we are interested to deal with the enhancement of the electrical properties of the optimum composition $Mn_{0.5}Ni_{0.1}Zn_{0.4}Fe_2O_4$

by substituting Cr^{3+} ions in octahedral B-site.

2. Materials and Methods

The $Mn_{0.5}Ni_{0.1}Zn_{0.4}Fe_{2-x}Cr_xO_4$ (where x = 0.0 - 0.4) samples were fabricated by standard solid-state reaction technique. High purity (99.9%) crushes of $MnCO_3$, NiO, ZnO, Cr_2O_3, and Fe_2O_3 were utilized as untreated substances for the synthesis of $Mn_{0.5}Ni_{0.1}Zn_{0.4}Fe_{2-x}Cr_xO_4$ compositions. The constituents in requisite stoichiometric amounts were mixed mechanically by hand milling in acetone media using a ceramic mortar for 6 hours and calcined in ambient air at 700°C for 3 hours. Afterward, the calcined powders were shaped into pellets and rings by a hydraulic press. After that, the samples were sintered at 1100°C, 1150°C and 1200°C for 3 hours. The temperature variation for sintering was 5°C/min during heating and 10°C/min during cooling. The compositions sintered at 1150°C were reserved for characterization based on optimum density. Some of these samples were polished for complex initial permeability and electrical characterization.

The XRD of the samples was performed using PHILIPS PW 3040 X'pert PRO X-ray diffractometer. The Nelson-Riley process was utilized for determining the precise a_0 of the samples. The Nelson-Riley (N-R) function $F(\theta)$ is specified by

$$F(\theta) = \frac{1}{2}\left(\frac{\cos^2\theta}{\sin\theta} + \frac{\cos^2\theta}{\theta}\right) \tag{1}$$

where θ demonstrates the Bragg angle. The values of a_0 for all the peaks of a sample were plotted as a function of $F(\theta)$. After that utilizing the least square fitting method precise lattice constants were found out. The point where the least square fitting straight line meets the y-axis (*i.e.* at $F(\theta)$ = 0) is the real a_0 of the sample.

Bulk density (ρ_B) of all the samples was measured by the formulae [16]:

$$\rho_B = \frac{m}{\pi r^2 t} \tag{2}$$

where m, r, and t represent the mass, radius, and thickness of the pellet or ring, individually. The X-ray density (ρ_x) was computed applying the following expression:

$$\rho_x = \frac{nM}{N_A V} \tag{3}$$

where n, M, N_A, and V reflect the number of atoms in a unit cell, the molar mass, Avogadro's number, and unit cell volume, separately. The porosity (P) was determined from the expression

$$P(\%) = \frac{\rho_x - \rho_B}{\rho_x} \times 100\% \tag{4}$$

The electromagnetic properties were characterized at ambient temperature as a function of frequency using WAYNE KERR 6500B Impedance Analyzer. The

μ_i' was calculated with the following relations [17]:

$$\mu_i' = \frac{L_s}{L_0} \tag{5}$$

$$\text{and} \quad L_0 = \frac{\mu_0 N^2 S}{\pi \bar{d}} \tag{6}$$

where, L_s is the self-inductance of the sample core and L_0 is the winding coil inductance in absence of sample core, N is the number of windings of the coil ($N = 5$), S is the cross-sectional area of the ring-shaped sample, $S = d \times h$, where, $d = \frac{d_2 - d_1}{2}$ and $\bar{d} = \frac{d_1 + d_2}{2}$ is the mean diameter of the ring-shaped sample. The RQF was settled from the ratio, $\frac{\mu_i'}{\tan \delta_M}$. The T_C of the compositions was computed from the temperature-controlled μ_i'.

For dielectric measurements, disk-shaped samples have been painted with silver paste on both sides for better electrical contact. The ε' was estimated using the given formula [3]:

$$\varepsilon' = \frac{C}{C_0} \tag{7}$$

$$\text{and} \quad \varepsilon'' = \varepsilon' \tan \delta_E \tag{8}$$

where C is the capacitance of the dielectric materials and $C_0 = \frac{\varepsilon_0 A}{t}$ is resulting geometrically. Here C_0 is the capacitance of the capacitor in the absence of dielectric specimens, ε_0 is the permittivity of free space ($\varepsilon_0 = 8.85 \times 10^{-12}$ Fm^{-1}), t is the thickness and $A \left(= \pi r^2 \right)$ is the cross-sectional area of the sample painted with silver paste.

Dielectric relaxation and conduction processes were accomplished in the complex modulus (M) spectra. The real (M') and imaginary (M'') segments of electric modulus were picked up from the dielectric data from the relations:

$$M' = \frac{\varepsilon'}{\varepsilon'^2 + \varepsilon''^2} \tag{9}$$

$$\text{and} \quad M'' = \frac{\varepsilon''}{\varepsilon'^2 + \varepsilon''^2} \tag{10}$$

3. Results and Discussion

3.1. X-Ray Diffraction, Lattice Constant, Density, and Porosity

XRD patterns for the samples $Mn_{0.5}Ni_{0.1}Zn_{0.4}Fe_{2-x}Cr_xO_4$ ($x = 0.0, 0.1, 0.2, 0.3, 0.4$) sintered at 1150°C for 3 hours are represented in **Figure 1**. The peaks in the XRD patterns disclose the single-phase spinel structure. The position of the XRD peaks is in good concurrence with other reports [17]. The a_0, density, and P of the samples are presented in **Table 1**. To find the precise value of a_0, all the values of a_0 are plotted against the N-R function. The exact value of a_0 of the sample is that point where the least square fitting straight line cuts the Y-axis. By plotting
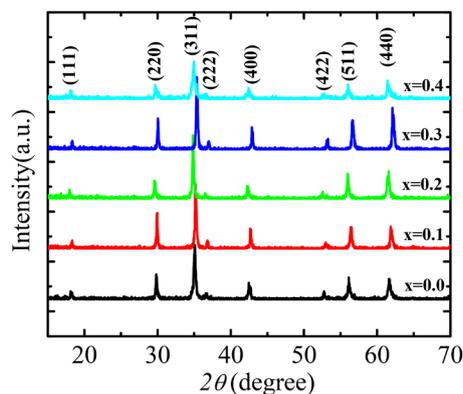
Figure 1. XRD patterns of different $Mn_{0.5}Ni_{0.1}Zn_{0.4}Fe_{2-x}Cr_xO_4$ ferrites.

Table 1. The a_0, ρ_B, ρ_x, P, and $\bar{D}$ of $Mn_{0.5}Ni_{0.1}Zn_{0.4}Fe_{2-x}Cr_xO_4$ ferrites.

Content (x)	a_0 (Å)	ρ_B (g/cm³)	ρ_x (g/cm³)	P (%)	$\bar{D}$ (µm)
0.0	8.51	4.70	5.21	9.79	0.0861
0.1	8.50	4.71	5.26	10.46	0.1280
0.2	8.52	4.63	5.29	12.48	0.1312
0.3	8.46	4.59	5.23	12.24	0.0846
0.4	8.52	4.49	5.22	13.98	0.0876
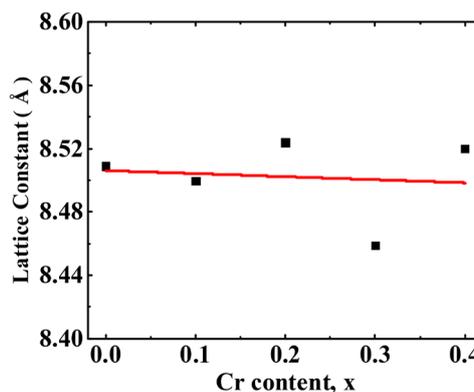
Figure 2. Lattice constant of $Mn_{0.5}Ni_{0.1}Zn_{0.4}Fe_{2-x}Cr_xO_4$ as a function of Cr content.

the a_0 against Cr content in **Figure 2**, it appears that the value of the a_0 drops up to $x = 0.3$ with increasing the value of Cr content showing inconsistency for $x = 0.2$ and then rises with Cr content. This drop of the a_0 with increasing Cr content establishes the fact that the a_0 is proportional to the rise of the ionic radius as the ionic radius of Cr^{3+} (0.64 Å) is less than that of Fe^{3+} (0.67 Å) [18]. After $x = 0.3$, the a_0 rises with increasing Cr content. The rise in the a_0 for a higher concentration of Cr was also observed by Li *et al.* [19] The rise in the a_0 for a higher concentration of Cr may be due to the fact that instead of trivalent the divalent Cr ion substitutes Fe^{2+} in the A-site which results in the increase of lattice constant as the lattice constant of Cr^{2+} is larger than that of Fe^{2+} [19]. Another possible reason is: the oxides of Cr reside at the grain boundary (as seen from the micro-

graphs in section 3.2) thereby obstructing the grain growth and exerts a stress on the unit cell. To compensate for the stress exerted by the grain boundary, the a_0 rises for higher Cr^{3+} concentration. The inconsistency from the declining trend for $x = 0.2$ may be caused by the inhomogeneous diffusion of Cr^{3+} in the lattice.

The alteration of ρ_B and X-ray density (ρ_x) of $Mn_{0.5}Ni_{0.1}Zn_{0.4}Fe_{2-x}Cr_xO_4$ is understood from **Figure 3**. It is perceived that the ρ_x rises with Cr content linearly up to $x = 0.2$ and this is because the reduction in the volume of the unit cell increases the density of the sample. Unit cell volume is calculated using the formula $V = a_0^3$. Unit cell volume is reduced with rising Cr content until $x = 0.2$ as it depends on the a_0 which is also reduced with reducing Cr content. From the graph, it is perceived that the ρ_x is higher than the ρ_B one which means that when the samples are sintered, they might contain cracks and pores on the microscopic scale and vacancies in the lattice on the atomic scale [20]. It is observed from **Table 1** that the variation of P of the sample behaves exactly in the opposite manner to that of the ρ_B. The ρ_B is diminished with increasing Cr^{3+} because the atomic mass of Cr^{3+} is less than that of Fe^{3+}. Moreover, the influence of the residual stress decreases the $\bar{D}$ and increases P.

3.2. Microstructure

For the morphological study, a microstructural image of Mn-Ni-Zn-Cr ferrite samples sintered at 1150°C was taken using FESEM (Model no. JEOL JSM 7600F) so that an insight of grain structure can be understood. The linear intercept technique was employed to determine the mean grain diameter of the samples.

It is evident from **Figure 4** that the $\bar{D}$ is increased with Cr content until $x = 0.2$ because the doped Cr_2O_3 becomes liquid phase in optimized oxygen potential and that liquid phase stimulates the grain growth. The $\bar{D}$ decreases for $x = 0.3$ and $x = 0.4$ which may be due to the fact that higher compounds can act as obstacles for visco-plastic deformation and Cr^{3+} resides at the grain boundary and hinders the grain growth. Grain growth and grain boundary mobility are very closely related to each other. Once the homogeneous driving force of grain
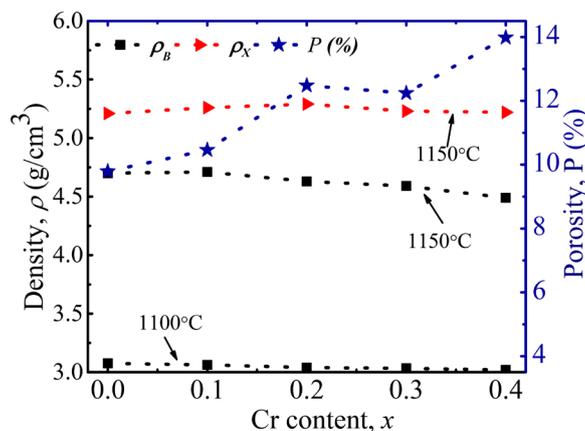

Figure 3. Variation of ρ_B, ρ_x, and P of $Mn_{0.5}Ni_{0.1}Zn_{0.4}Fe_{2-x}Cr_xO_4$ ferrites as a function of Cr content.
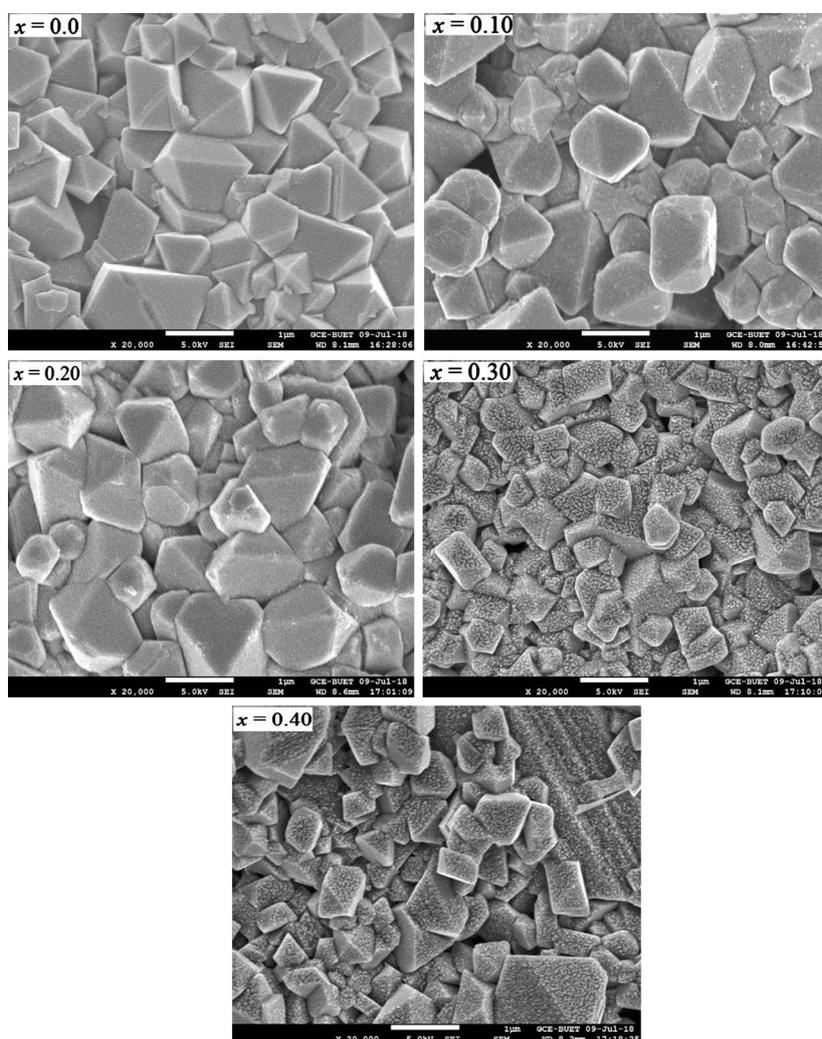
Figure 4. FESEM images of various $Mn_{0.5}Ni_{0.1}Zn_{0.4}Fe_{2-x}Cr_xO_4$ ferrites.

boundary is attained, the sintered body achieves a unified grain size distribution. The compositional variation of the samples affects the grain size distribution. The grain size reflects the presence of a lesser grain boundary area. The pores are left behind the fast-moving grain boundaries and are confined within the grains only when the grain expansion rate is very high.

3.3. Magnetic Characterization

3.3.1. Complex Initial Permeability

The μ_i' provides a precise description of the stored energy by expressing magnetic induction with the magnetic field. The μ_i' has been measured against frequency in the range 10 kHz - 120 MHz at ambient temperature for all the samples of the series $Mn_{0.5}Ni_{0.1}Zn_{0.4}Fe_{2-x}Cr_xO_4$. From **Figure 5**, it is noted that with the rise in frequency, the μ_i' remains stable up to a particular frequency, and after that μ_i' falls rapidly. Generally, the ferri-magnetic order of ferrite develops from anti-parallel and unequal spin moments in the neighboring magnetic sub-lattices which is determined by the distribution of the transition metal

ions [21]. A substantial amount of Fe^{3+} ions reside in the octahedral sub-lattice in $Mn_{0.5}Ni_{0.1}Zn_{0.4}Fe_{2-x}Cr_xO_4$. So, the Cr^{3+} ion leads the Fe^{3+} ions to enter into the tetrahedral sub-lattice. Thus the doped sample will show the antiferromagnetic character and the remarkable reduction of μ_i' with the rise of Cr^{3+} results due to this antiferromagnetic behavior of the samples as in **Figure 5**.

The frequency dependence of the magnetic loss tangent ($\tan\delta_M$) of the composition $Mn_{0.5}Ni_{0.1}Zn_{0.4}Fe_{2-x}Cr_xO_4$ sintered at 1150°C at ambient temperature over the range 10 kHz - 120 MHz is illustrated in **Figure 6**. The value of $\tan\delta_M$ decreases with frequency arriving at the lowest value and after that becomes nearly constant. The grounds behind reducing $\tan\delta_M$ with increasing frequency is that, beyond the definite frequency of the electric field, the domain wall motion cannot go along with the external electric field. It is perceived that the $\tan\delta_M$ reduces significantly with the Cr content at a very high frequency. The low value of the $\tan\delta_M$ is the main requirement for the high-frequency magnetic application [16].

The frequency dependence of the RQF of the compositions of $Mn_{0.5}Ni_{0.1}Zn_{0.4}Fe_{2-x}Cr_xO_4$ sintered at 1150°C at ambient temperature over the range 10 kHz - 120 MHz is illustrated in **Figure 7**. It is perceived that RQF enhances with frequency and after a certain frequency RQF slightly reduces with the rise of frequency.
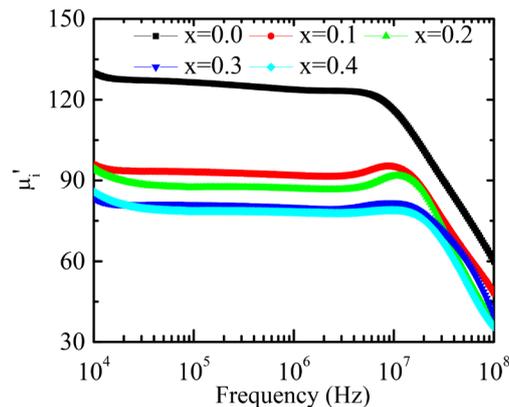

Figure 5. Variation of μ_i' of $Mn_{0.5}Ni_{0.1}Zn_{0.4}Fe_{2-x}Cr_xO_4$ ferrites as a function of frequency.
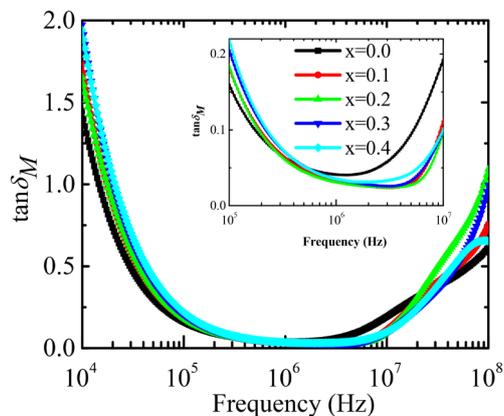
Figure 6. Variation of $\tan\delta_M$ of $Mn_{0.5}Ni_{0.1}Zn_{0.4}Fe_{2-x}Cr_xO_4$ ferrites as a function of frequency.

RQF has the highest magnitude at a certain frequency where the $\tan\delta_M$ has the lowest magnitude [22]. RFQ's improvement can be attributed to the 10% of Cr addition and this addition is expected to decrease the M_s. The RQF is often used as a measure of performance for inductors used in filtering action.

3.3.2. Temperature-Dependent Complex Initial Permeability

Curie temperature (T_c) measurement is one of the most significant measurements for magnetic materials. The T_c gives substantial information on the magnetic status of a substance for the strength of exchange interaction. The temperature-dependent μ_i' for $Mn_{0.5}Ni_{0.1}Zn_{0.4}Fe_{2-x}Cr_xO_4$ is depicted in **Figure 8**. The μ_i' is measured at a fixed frequency of 100 kHz. The μ_i' drops rapidly at the temperature when the magnetism of the samples shifts from ferromagnetic to paramagnetic (at Curie point). The sharp fall of μ_i' with temperature represents the degree of homogeneity of the samples [23] [24]. In the present case instead of sharp fall μ_i' drops rapidly owing to the presence of crack and pores within the samples. It is revealed from **Figure 8** that when Cr^{3+} is doped in $Mn_{0.5}Ni_{0.1}Zn_{0.4}Fe_2O_4$, T_c decreases. The decline in T_C is mainly attributable to the weakening of the A-B interaction, which is confirmed from that the ionic radius of Cr^{3+} (0.64 Å) is less than Fe^{3+} (0.67 Å). Due to the replacement of Fe^{3+} by Cr^{3+}, the longest distance between moments causes a decrease in A-B interaction in
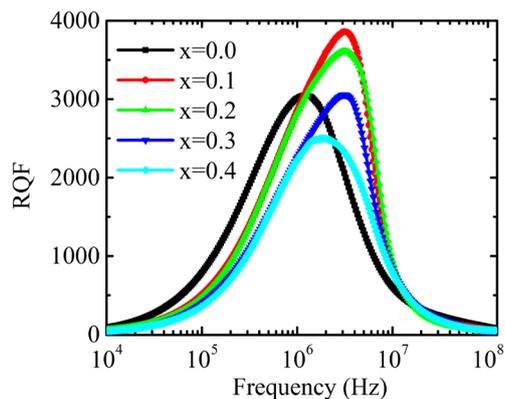

Figure 7. Variation of RQF of $Mn_{0.5}Ni_{0.1}Zn_{0.4}Fe_{2-x}Cr_xO_4$ ferrites as a function of frequency.
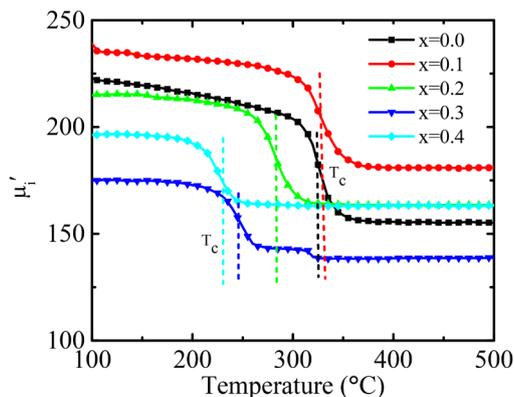
Figure 8. Variation of μ_i' with temperature of $Mn_{0.5}Ni_{0.1}Zn_{0.4}Fe_{2-x}Cr_xO_4$ ferrites.

the $Mn_{0.5}Ni_{0.1}Zn_{0.4}Fe_2O_4$ relative to all other samples, and consequently, T_c decreases [4].

3.3.3 Magnetic Hysteresis Loop

Measurement of magnetic hysteresis loop and magnetization for all the samples of $Mn_{0.5}Ni_{0.1}Zn_{0.4}Fe_{2-x}Cr_xO_4$ were carried out by using Vibrating Sample Magnetometer. Observation of **Figure 9** showed that M_s reduces with the rise of Cr^{3+} concentration. This happens since the substituted Cr^{3+} ion has a site preference to occupy B-site which makes the iron enter into the A-site from B-site. As a consequence, the exchange interaction between A and B sites turns weaker resulting in intensifying the B-B interaction and weakening the A-B interaction, which in turn reduces the M_s of the samples. Besides, Cr has less magnetic moment than Fe, which may be another reason for the reduction of magnetization with Cr content. Similar results were reported in other reports [25] [26]. The samples having $x = 0.1$ confirmed improved ferromagnetic property as shown in **Table 2**.

3.4. Electrical Characterization

3.4.1. Dielectric Property

The variation of frequency-dependent ε' of $Mn_{0.5}Ni_{0.1}Zn_{0.4}Fe_{2-x}Cr_xO_4$ at ambient temperature is illustrated in **Figure 10**. It can be realized that the ε' drops rapidly with a rise in frequency thereby showing dispersion in the low-frequency range
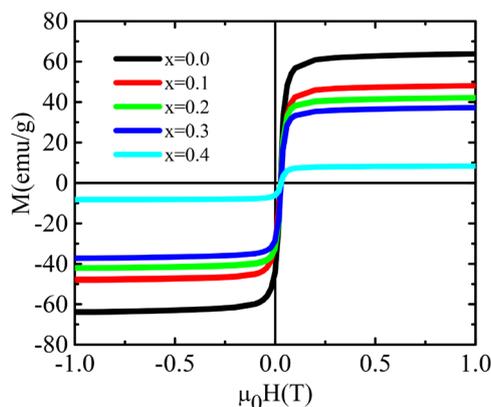
Figure 9. *M-H* loops of $Mn_{0.5}Ni_{0.1}Zn_{0.4}Fe_{2-x}Cr_xO_4$ ferrites at room temperature.

Table 2. The M_s, coercivity (H_c), K, remanent magnetization (M_r) of $Mn_{0.5}Ni_{0.1}Zn_{0.4}Fe_{2-x}Cr_xO_4$ ferrites.

Content, (x)	M_s (emu/g)	H_c (T)	K	M_r (emu/g)
0.0	61.58	2.241	69.00	0.169
0.1	46.31	4.367	101.118	0.213
0.2	41.22	1.928	39.73	0.282
0.3	36.09	2.206	39.80	0.079
0.4	8.31	4.697	19.52	0.071
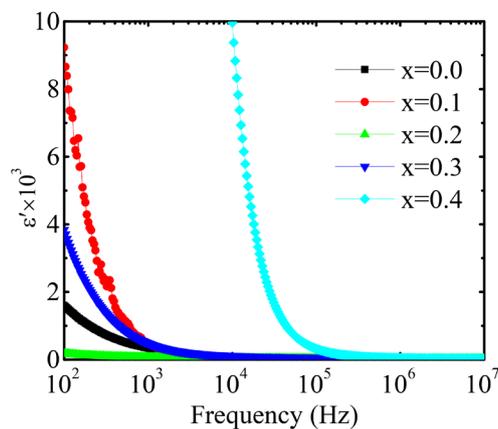
Figure 10. Variation of ε' for various $Mn_{0.5}Ni_{0.1}Zn_{0.4}Fe_{2-x}Cr_xO_4$ ferrites as a function of frequency.
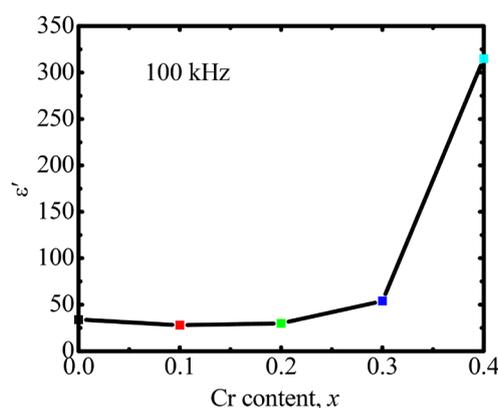
Figure 11. Variation of ε' with Cr content of $Mn_{0.5}Ni_{0.1}Zn_{0.4}Fe_{2-x}Cr_xO_4$ ferrites.

and become constant at the high-frequency range. The observed dispersion at lower frequencies can be interpreted applying Maxwell-Wagner interfacial polarization which plays a crucial role in such a heterogeneous system [27] [28] [29]. The high values of ε' observed at low-frequency range are because of the presence of the heterogeneity in the composition. Heterogeneities in the samples initiate space charge polarization and contribute towards the high values of ε'. As Cr content rises, the amount of space charge also rises. The reduction of Fe^{3+} concentration causes the transport of some Mn^{2+} in the octahedral site which causes an enhancement of hopping charge carriers and consequently provides a high value of ε'. **Figure 11** displays the variation of ε' with Cr content at a frequency of 100 kHz. The highest ε' is obtained for the sample with $x = 0.4$. The grain boundary impedance decreases due to the presence of the second phase in between grains for high Cr content which in turn increases ε'.

The variation of $\tan\delta_E$ as a function of the frequency of the composition $Mn_{0.5}Ni_{0.1}Zn_{0.4}Fe_{2-x}Cr_xO_4$ is shown in **Figure 12** sintered at 1150°C. The $\tan\delta_E$ unveils the similar nature of ε'. This means that at low frequency the $\tan\delta_E$ is high and drops with frequency. The $\tan\delta_E$ is proportional to the "loss of energy" from the applied field in the ferrite (in fact this energy is wasted as heat) and

hence designated as a $\tan\delta_E$. The $\tan\delta_E$ arises in materials due to the phase difference between polarization and applied field in the high-frequency region.

3.4.2. AC Resistivity

The significant electrical property resistivity is an intrinsic property of magnetic material. The resistivity of $Mn_{0.5}Ni_{0.1}Zn_{0.4}Fe_{2-x}Cr_xO_4$ sintered at 1150˚C was calculated and plotted against frequency as shown in Figure 13. It is observed that AC resistivity also shows significant dispersion as ε' at lower frequencies due to the dominant space charge polarization. At low-frequency AC resistivity rises with Cr content up to $x = 0.2$ and then reduces with a further rise of Cr content because the ε' is high for samples with higher Cr concentration *i.e.*, for $x = 0.3$ and $x = 0.4$. It is found that ac resistivity reduces with frequency showing significant dispersion and this dispersion is more at low-frequency range which might be due to the variation in the concentration of Fe^{3+}/Fe^{2+} and other ions in various samples [30].

3.5. Complex Impedance Spectra Analysis

Transport properties are strongly dependent on microstructure in polycrystalline solids, and impedance spectra generally include functionalities that may be
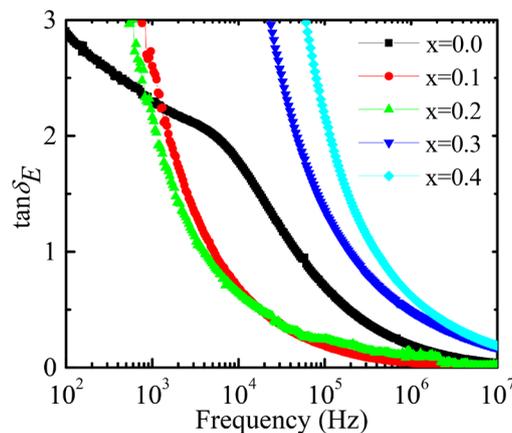

Figure 12. Variation of $\tan\delta_E$ of $Mn_{0.5}Ni_{0.1}Zn_{0.4}Fe_{2-x}Cr_xO_4$ ferrites as a function of frequency.
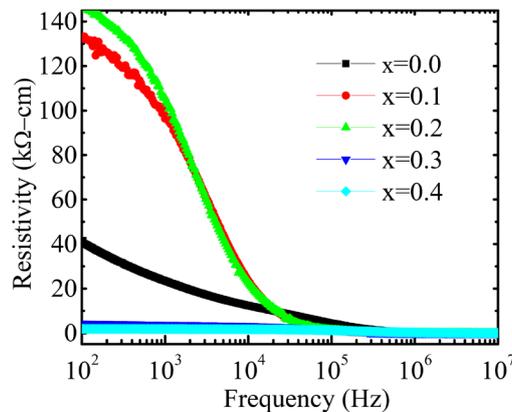
Figure 13. Resistivity of various $Mn_{0.5}Ni_{0.1}Zn_{0.4}Fe_{2-x}Cr_xO_4$ ferrites as a function of frequency.

specifically linked to microstructure. **Figure 14(a)** demonstrates the alteration of resistance (Z') with the frequency of the samples at ambient temperature. The higher value of Z' at lower frequency is due to the dominant space charge polarization [31]. Observation confirms that with the rise in frequency up to a specific limit (~1 kHz), the value of Z' rapidly decreases which means conductivity of the ferrite samples increases [32]. As all types of polarization are present at the lower frequency it gives higher magnitudes of Z'. But at the high-frequency region, the values of Z' decreases as the contribution from different parts of polarization ceases, this is because only electronic polarization can carry over the fast variation of field frequency [33] [34]. The alteration of reactance (Z'') with the frequency is illustrated in **Figure 14(b)**. The frequency dependence of Z'' [**Figure 14(b)**] behaves similarly as Z' in addition to the appearance of some relaxation peaks due to immobile charges.

According to the brick-layer model, an equivalent circuit comprising of three parallel *RC* circuits can explain polycrystalline ceramics [35]. Each *RC* component of the equivalent circuit produces a semicircle in the Z' vs Z'' plot (Cole-Cole diagram). A single semicircle at a higher frequency in Z' vs Z'' plot specifies grain effect, the second semicircle at a lower frequency specifies the presence of grain boundary effect, and a third semicircular arc or spike is often observed which is due to the electrode effect. **Figure 15** represents the Cole-Cole plot of various $Mn_{0.5}Ni_{0.1}Zn_{0.4}Fe_{2-x}Cr_xO_4$ ferrites. It is noticed that the first two compositions ($x = 0.0$ and 0.1) show two semicircular arcs one at high frequency for grain interior and another at a lower frequency for grain boundary effect. The rest of the compositions show a single semicircular arc that specifies the materials have only grain contribution to the conduction process as the semicircle appearing at higher frequency correlates to the resistance of grain only but the semicircle at low frequency is because of the resistance of grain boundaries [36]. The grain boundary impedance arises due to the random alignment of grains existing two-dimensional conductivity. The non-existence of grain boundary impedance for $x = 0.2$, 0.3, and 0.4 may be due to the presence of the second phase dispersed along the grain boundary area which efficiently short
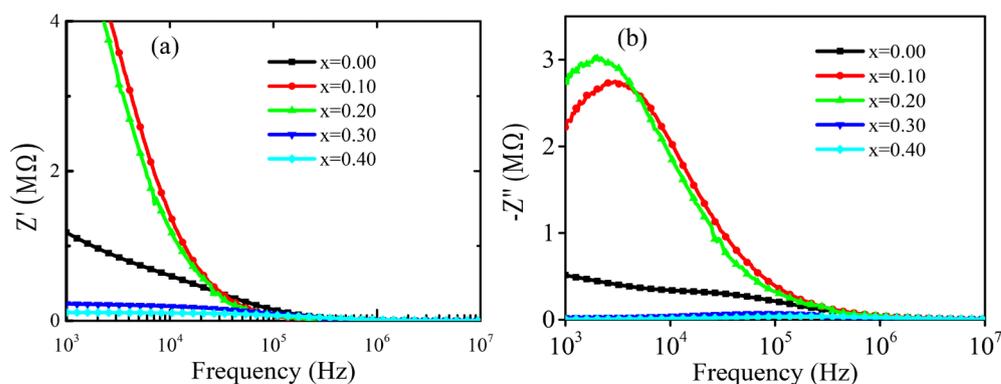

Figure 14. Variation of (a) Z' and (b) Z'' of $Mn_{0.5}Ni_{0.1}Zn_{0.4}Fe_{2-x}Cr_xO_4$ ferrites as a function of frequency.
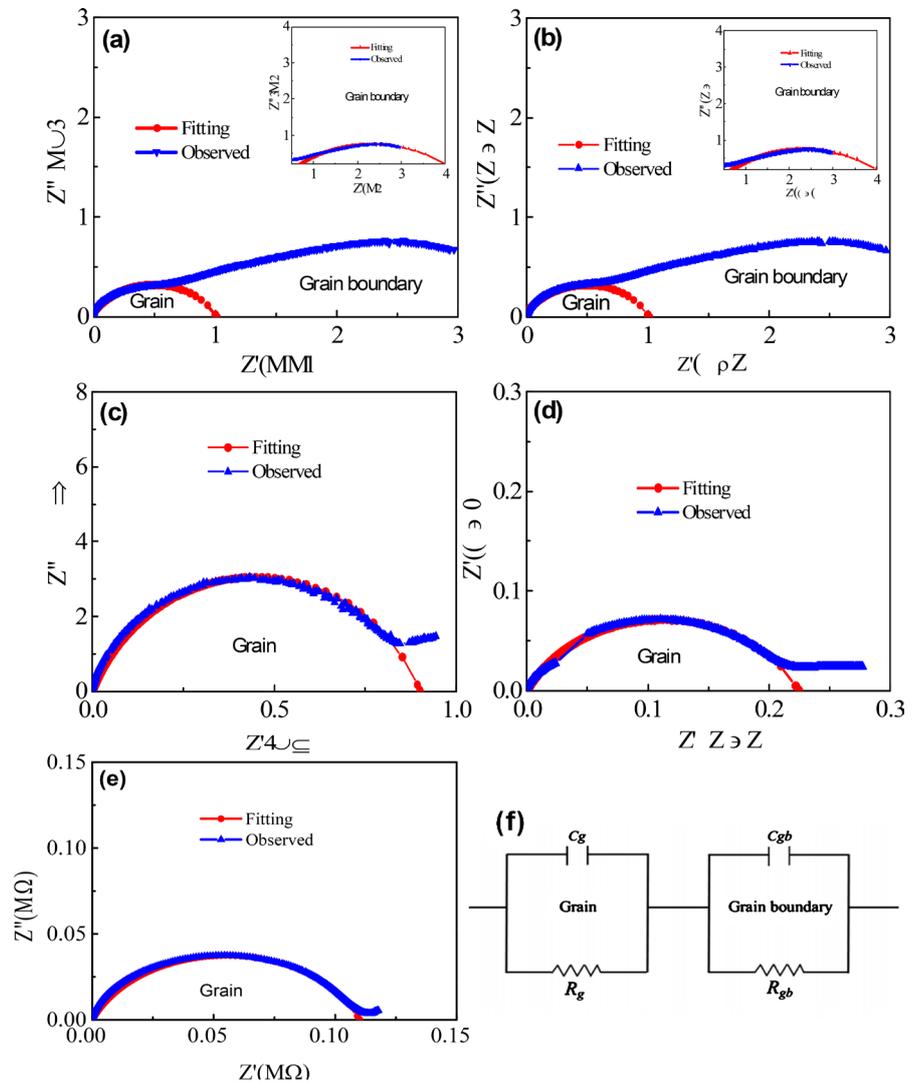
Figure 15. Nyquist plots of different $Mn_{0.5}Ni_{0.1}Zn_{0.4}Fe_{2-x}Cr_xO_4$ ferrites: (a) $x = 0.0$, (b) $x = 0.1$, (c) $x = 0.2$, (d) $x = 0.3$ and (e) $x = 0.4$ samples, and (f) equivalent circuit [39].

circuits the grain boundary impedance. Depressed semicircular arcs are perceived for every composition. Experimentally it is unusual to find a complete semicircle with its center lying on the axis of the Z'. The agitations which result in depressed semicircular arcs in the Z' axis are: 1) the arcs do not go through the origin because of the presence of other arcs at high frequency and/or the bulk resistance is larger than zero, 2) the centers of the investigational arcs are often relocated below the real axis due to the occurrence of dispersed elements in the material–electrode arrangement [37]. Therefore the relaxation time (τ) is not single-valued and is spread constantly or separately across a mean $\tau_m \left(= \omega_m^{-1} \right)$ and 3) arcs might be considerably twisted by additional relaxations. The arcs at higher frequency side constitute bulk resistance and those at the lower frequency side constitute grain boundary resistance [38] [39]. These responses can be explained by an equivalent circuit comprising of two sub-circuits attached in series as depicted in **Figure 15(f)** [39]. In general, the impedance is expressed as:

Table 3. The ε', grain, and grain boundary resistances of various $Mn_{0.5}Ni_{0.1}Zn_{0.4}Fe_{2-x}Cr_xO_4$ ferrites.

Composition	x = 0.0	x = 0.1	x = 0.2	x = 0.3	x = 0.4
ε' at 100 kHz	35	26	29	55	316
R_g(KΩ)	1009	1009	899	224	110
R_{gb}(KΩ)	3267	3250	0	0	0

$$Z^* = R_g - 1/jwC_g + R_{gb} - 1/jwC_{gb} \qquad (11)$$

where R_g is the grain resistance, C_g is the grain capacitance, R_{gb} is the grain boundary resistance and C_{gb} is the grain boundary capacitance. The arcs in low and high-frequency areas conform to $R_{gb}C_{gb}$ and R_gC_g responses, respectively. The grain resistance decreases rapidly with the rise in Cr^{3+} in the composition (Table 3) due to the increased space charge polarization.

4. Conclusion

The XRD patterns identified a single-phase spinel ferrite structure. The FESEM images revealed that the $\overline{D}$ of the samples increased up to $x = 0.2$ owing to the development of Cr_2O_3 liquid phase which promoted the grain growth and after $x = 0.2$, $\overline{D}$ decreased due to the shrinkage of the lattice. Among the studied samples, it is clear that 10% of Cr^{3+} doped sample has the highest ε' with low loss, highest AC resistivity, good magnetizing capability, and highest RQF. The well saturated magnetic hysteresis loop indicated the ferromagnetic character of the present samples. The T_C is found to be decreased with Cr content in the composition resulting from the smaller ionic radius of Cr than Fe. The impedance spectra analysis established a close correlation of the conduction mechanism with the microstructure of the samples. Both grain and grain boundaries contributed to the total conduction process for the first two compositions. The rest of the compositions had only grain contribution to the conduction process because the second phase dispersed along the grain boundary area efficiently short-circuited the grain boundary impedance. As in the field of electronics and communication devices have to deal with electric as well as magnetic properties, this ferrite composition may be used for the fabrication of different electronic and communication devices.

Acknowledgements

Conflicts of Interest

The authors declare no conflicts of interest regarding the publication of this paper.

References

[1] Sivakumar, N., Narayanasamy, A., Ponpandian, N. and Govindaraj, G. (2007) Grain Size Effect on the Dielectric Behavior of Nanostructured $Ni_{0.5}Zn_{0.5}Fe_2O_4$. *Journal of Applied Physics*, **101**, 084116. https://doi.org/10.1063/1.2721379

[2] Hossain, A.K.M.A., Mahmud, S.T., Seki, M., Kawai, T. and Tabata, H. (2007) Structural, Electrical Transport, and Magnetic Properties of $Ni_{1-x}Zn_xFe_2O_4$. *Journal of Magnetism and Magnetic Materials*, **312**, 210-219. https://doi.org/10.1016/j.jmmm.2006.09.030

[3] Goldman, A. (1999) Handbook of Modern Ferromagnetic Materials. Kulwer Academic Publishers, Boston. https://doi.org/10.1007/978-1-4615-4917-8

[4] Valenzuela, R. (1994) Magnetic Ceramics. Cambridge University Press, Cambridge. https://doi.org/10.1017/CBO9780511600296

[5] Chukalkin, Y.G. and Teplykh, A.E. (1998) Magnetic State of Nickel-Zinc Ferrites at High Zinc Concentrations. *Physics of the Solid State*, **40**, 1364-1365. https://doi.org/10.1134/1.1130559

[6] Mahmud, S.T., Akther Hossain, A.K.M., Abdul Hakim, A.K.M., Seki, M., Kawai, T. and Tabata, H. (2006) Influence of Microstructure on the Complex Permeability of Spinel Type Ni-Zn Ferrite. *Journal of Magnetism and Magnetic Materials*, **305**, 269-274. https://doi.org/10.1016/j.jmmm.2006.01.012

[7] Rezlescu, N., Rezlescu, E., Pasnicu, C. and Craus, M.L. (1994) Effects of the Rare-Earth Ions on Some Properties of a Nickel-Zinc Ferrite. *Journal of Physics: Condensed Matter*, **6**, 5707-5716. https://doi.org/10.1088/0953-8984/6/29/013

[8] Rezlescu, E., Sachelarie, L., Popa, P.D. and Rezlescu, N. (2000) Effect of Substitution of Divalent Ions on the Electrical and Magnetic Properties of Ni-Zn-Me Ferrites. *IEEE Transactions on Magnetics*, **36**, 3962-3967. https://doi.org/10.1109/20.914348

[9] Singh, A.K., Goel, T.C., Mendiratta, R.G., Thakur, O.P. and Prakash, C. (2002) Magnetic Properties of Mn-Substituted Ni-Zn Ferrites. *Journal of Applied Physics*, **92**, 3872-3876. https://doi.org/10.1063/1.1504493

[10] Singh, A.K., Goel, T.C. and Mendiratta, R.G. (2004) Low-Temperature Synthesis of $Mn_{0.2}Ni_{0.2}Zn_{0.6}Fe_2O_4$ Ferrites by Citrate Precursor Method and Study of Their Properties. *Physica Status Solidi (a)*, **201**, 1453-1457. https://doi.org/10.1002/pssa.200306775

[11] Singh, A.K., Goel, T.C. and Mendiratta, R.G. (2003) Effect of Manganese Impurity on the Conductivity, Dielectric Behavior and Magnetic Properties of $Ni_{0.3}Mn_xZn_{0.7-x}Fe_2O_4$. *Japanese Journal of Applied Physics*, **42**, 2690-2691. https://doi.org/10.1143/JJAP.42.2690

[12] Sattar, A.A., El-Sayed, H.M., El-Shokrofy, K.M. and El-Tabey, M.M. (2005) Improvement of the Magnetic Properties of Mn-Ni-Zn Ferrite by the Non Magnetic Al-Ion Substitution. *Journal of Applied Science*, **5**, 162.

[13] Sattar, A.A., El-Sayed, H.M., El-Shokrofy, K.M. and El-Tabey, M.M. (2005) Effect of Manganese Substitution on the Magnetic Properties of Nickel-Zinc Ferrite. *Journal of Materials Engineering and Performance*, **14**, 99-103. https://doi.org/10.1361/10599490522185

[14] Kulkarni Suresh, R. (2012) Development of In^{3+} Substituted Mn-Ni-Zn Nanoferrite Core Material. *Archives of Physics Research*, **3**, 116.

[15] Eltabey, M.M., Agami, W.R. and Mohsen, H.T. (2014) Improvement of the Magnetic Properties for Mn-Ni-Zn Ferrites by Rare Earth Nd^{3+} Ion Substitution. *Journal*

of Advanced Research, **5**, 601-605. https://doi.org/10.1016/j.jare.2013.08.005

[16] Cullity, B.D. (1972) Introduction to Magnetic Materials. Addison-Wisley Publishing Company, Inc., Menlo Park.

[17] Mane, D.R., Birajdar, D.D., Shirsath, S.E., Telugu, R.A. and Kadam, R.H. (2010) Structural and Magnetic Characterizations of Mn-Ni-Zn Ferrite Nanoparticles. *Physica Status Solidi* (*a*), **207**, 2355-2363. https://doi.org/10.1002/pssa.201026079

[18] Vegard, L. (1921) Die Konstitution der Mischkristalle und die Raumfüllung der Atome. *Zeitschrift für Physik*, **5**, 17-26. https://doi.org/10.1007/BF01349680

[19] Li, Z., Dai, J., Cheng, C., Suo, Z. and Qing, W. (2020) Synthesis and Magnetic Properties of Chromium Doped Cobalt Ferrite Nanotubes. *Materials Research Express*, **7**, 086102. https://doi.org/10.1088/2053-1591/abae26

[20] Cullity, B.D. and Stock, S.R. (2001) Elements of X-Ray Diffraction. 3rd Edition, Prentice Hall, Upper Saddle River.

[21] Xu, F., Bai, Y., Ai, F. and Qiao, L.J. (2008) The Magnetic and Dielectric Properties of Multiferroic Sr-Substituted Zn_2-Y Hexagonal Ferrites. *Chinese Physics B*, **17**, 4652-4655. https://doi.org/10.1088/1674-1056/17/12/054

[22] Overshott, K. (1981) The Causes of the Anomalous Loss in Amorphous Ribbon Materials. *IEEE Transactions on Magnetics*, **17**, 2698-2700. https://doi.org/10.1109/TMAG.1981.1061648

[23] Cedillo, E., Ocampo, J., Rivera, V. and Valenzuela, R. (1980) An Apparatus for the Measurement of Initial Magnetic Permeability as a Function of Temperature. *Journal of Physics E: Scientific Instruments*, **13**, 383-386. https://doi.org/10.1088/0022-3735/13/4/005

[24] Valenzuela, R. (1980) A Sensitive Method for the Determination of the Curie Temperature in Ferrimagnets. *Journal of Materials Science*, **15**, 3173-3174. https://doi.org/10.1007/BF00550394

[25] Alam, F., Rahman, M.L., Khan, M.H.R. and Hossain, A.K.M.A. (2014) Magnetic Hysteresis and Complex Initial Permeability of Cr^{3+} Substituted Mn-Zn Ferrites. *Journal of Modern Physics*, **5**, 1223-1233. https://doi.org/10.4236/jmp.2014.514122

[26] Guilland, C. and Creveaux, H. (1950) *Comptes Rendus de l' Académie des Sciences*, **230**, 1256.

[27] Mazumdar, S.C., Khan, M.N.I., Islam, M.F. and Hossain, A.K.M.A. (2015) Enhanced Multiferroic Properties in $(1-y)BiFeO_{3-y}Ni_{0.50}Cu_{0.05}Zn_{0.45}Fe_2O_4$ Composites. *Journal of Magnetism and Magnetic Materials*, **390**, 61-69. https://doi.org/10.1016/j.jmmm.2015.04.087

[28] Maxwell, J.C. (1973) Electricity and Magnetism. Oxford University Press, London.

[29] Chougule, S.S. and Chougule, B.K. (2008) Response of Dielectric Behavior and Magnetoelectric Effect in Ferroelectric Rich $(x)Ni_{0.9}Zn_{0.1}Fe_2O_4+(1-x)PZT$ ME Composites. *Journal of Alloys and Compounds*, **456**, 441-446. https://doi.org/10.1016/j.jallcom.2007.02.089

[30] Yang, H., Wang, H., He, L., Shui, L. and Yao, X. (2010) Polarization Relaxation Mechanism of $Ba_{0.6}Sr_{0.4}TiO_3/Ni_{0.8}Zn_{0.2}Fe_2O_4$ Composite with Giant Dielectric Constant and High Permeability. *Journal of Applied Physics*, **108**, 074105. https://doi.org/10.1063/1.3490782

[31] Dhak, P., Dhak, D., Das, M., Pramanik, K. and Pramanik, P. (2009) Impedance Spectroscopy Study of $LaMnO_3$ Modified $BaTiO_3$ Ceramics. *Materials Science and Engineering: B*, **164**, 165-171. https://doi.org/10.1016/j.mseb.2009.09.011

[32] Brahma, S., Choudhary, R.N.P. and Thakur, A.K. (2005) AC Impedance Analysis of LaLiMo$_2$O$_8$ Electroceramics. *Physica B: Condensed Matter*, **355**, 188-201. https://doi.org/10.1016/j.physb.2004.10.091

[33] Behera, B., Nayak, P. and Choudhary, R. (2008) Structural and Electrical B. Behera, P. Nayak, R.N.P. Choudhary, Structural and Electrical Properties of KCa$_2$Nb$_5$O$_{15}$ Ceramics. *Central European Journal of Physics*, **6**, 289-295. https://doi.org/10.2478/s11534-008-0030-4

[34] Intatha, U., Eitssayeam, S., Wang, J. and Tunkasiri, T. (2010) Impedance Study of Giant Dielectric Permittivity in BaFe$_{0.5}$Nb$_{0.5}$O$_3$ Perovskite Ceramic. *Current Applied Physics*, **10**, 21-25. https://doi.org/10.1016/j.cap.2009.04.006

[35] MacDonald, J.R. (1987) Impedance Spectroscopy. Wiley-Interscience, New York.

[36] Behera, C., Choudhary, R.N.P. and Das, P.R. (2016) Structural, Dielectric, Impedance and Magneto-Electric Properties of Mechanically Synthesized (Bi$_{0.5}$Ba$_{0.25}$Sr$_{0.25}$)(Fe$_{0.5}$Ti$_{0.5}$)O$_3$ Nano-Electronic System. *Materials Research Express*, **3**, 035005. https://doi.org/10.1088/2053-1591/3/3/035005

[37] Barsoukov, E. and Macdonald, J.R. (2005) Impedance Spectroscopy: Theory, Experiment, and Applications. John Wiley & Sons, Inc., Hoboken. https://doi.org/10.1002/0471716243

[38] Das, M.K., Zubair, M.A., Tanaka, H. and Hossain, A.K.M.A. (2020) Study of Impedance and Magnetoelectric Property of Lead-Free xLCNZFO+(1-x)BGTDO Multiferroic Composites. *Materials Chemistry and Physics*, **255**, 123575. https://doi.org/10.1016/j.matchemphys.2020.123575

[39] Mazumdar, S.C., Khan, M.N.I., Islam, M.F. and Hossain, A.K.M.A. (2016) Tuning of Magnetoelectric Coupling in (1−y)Bi$_{0.8}$Dy$_{0.2}$FeO$_3$-yNi$_{0.5}$Zn$_{0.5}$Fe$_2$O$_4$ Multiferroic Composites. *Journal of Magnetism and Magnetic Materials*, **401**, 443-454. https://doi.org/10.1016/j.jmmm.2015.10.051